Astronomy & Astrophysics manuscript no. output
August 23, 2019

Softly X-raying the γ-ray sky I.

Searching for the X-ray - γ-ray connection for *Fermi* BL Lac objects

E. J. Marchesini[1,2,3,4,5], A. Paggi[1], F. Massaro[1], N. Masetti[5,6], R. D'Abrusco[7], I. Andruchow[2,4], and R. de Menezes[1,8]

[1] Dipartimento di Fisica, Università degli Studi di Torino, via Pietro Giuria 1, I-10125 Turin, Italy
[2] Facultad de Ciencias Astronómicas y Geofísicas, Universidad Nacional de La Plata, Paseo del Bosque, B1900FWA, La Plata, Argentina
[3] INFN – Istituto Nazionale di Fisica Nucleare, Sezione di Torino, via Pietro Giuria 1, I-10125 Turin, Italy
[4] Instituto de Astrofísica de La Plata, CONICET–UNLP, CCT La Plata, Paseo del Bosque, B1900FWA, La Plata, Argentina
[5] INAF – Osservatorio di Astrofisica e Scienza dello Spazio, via Gobetti 93/3, I-40129, Bologna, Italy
[6] Departamento de Ciencias Fisicas, Universidad Andres Bello, Fernandez Concha 700, Las Condes, Santiago, Chile
[7] Center for Astrophysics | Harvard & Smithsonian , 60 Garden St, Cambridge (MA) 02138, USA
[8] Universidade de São Paulo, Instituto de Astronomia, Geofísica e Ciências Atmosféricas, Departamento de Astronomia, São Paulo, SP 05508-090, Brazil

ABSTRACT

Context. BL Lac objects are an extreme type of active galactic nuclei (AGNs) belonging to the largest population of gamma-ray sources: blazars. This class of AGNs shows a double-bumped SED usually described in terms of Synchrotron-Self-Compton (SSC) emission process whereas the low energy component, dominating their emission between the infrared and the X-ray band, is tightly connected to the high energy one peaking in the gamma-rays. Two strong connections, linking radio and mid-infrared emission of blazars to that in the gamma-ray band are well established. They constitute the basis to associate gamma-ray sources with their low energy counterparts.
Aims. In this work, we searched for a possible link between X-ray and gamma-ray emissions for the subclass of BL Lacs using all archival Swift/XRT observations combined with the Fermi data for a selected sample of 351 sources.
Methods. Analyzing ∼2400 ks of Swift/XRT observations carried out until December 2018, we discovered that, above the γ-ray flux threshold $F_\gamma \approx 3 \times 10^{-12}$ erg cm^{-2} s^{-1}, 96% of all *Fermi* BL Lacs have an X-ray counterpart detected with signal-to-noise ratio grater than 3.
Results. We did not find any correlation or neat trend between X-ray and gamma-ray fluxes and/or spectral shapes, however we discovered a correlation between the X-ray flux and the mid-infrared color. Finally, we discuss on a possible interpretation of our results in the SSC framework.

1. Introduction

Blazars are a peculiar class of active galactic nuclei (AGNs) characterized by emission arising from a relativistic jet oriented at small angles (e.g. less than a few degrees, Lister et al. 2013) with respect to the line of sight, that overwhelms most of the radiation of their host galaxy (Blandford & Rees 1978).

Blazar emission is detected at all frequencies, from radio (see e.g., Jorstad et al. 2001; Ciaramella et al. 2004; Ghirlanda et al. 2010; Lister et al. 2019), even at low radio frequencies (see e.g., Nori et al. 2014; Giroletti et al. 2016, for recent observational campaigns), infrared (IR, see e.g., Impey & Neugebauer 1988; Stevens et al. 1994; Massaro et al. 2011a; D'Abrusco et al. 2012) and optical (see e.g., Carini et al. 1992; Marchesini et al. 2016; Peña-Herazo et al. 2017a; Marchesini et al. 2019a, for recent observational campaigns) up to X-rays (see e.g., Singh & Garmire 1985; Giommi et al. 1990; Sambruna et al. 1996; Pian et al. 1998; Paggi et al. 2013; Landi et al. 2015). They are also detected in the gamma-ray band (see e.g., Aharonian et al. 2005; Albert et al. 2007; Giannios et al. 2009; Tavecchio et al. 2011; Wehrle et al. 1998; Ackermann et al. 2015), and show strong variability and occurrence of flaring states, changing both spectral shape and/or luminosities (see e.g., Hartman et al. 2001; Romero et al. 2002; Böttcher et al. 2007; Pandey et al. 2017; Kaur et al. 2017; Bruni et al. 2018).

Blazars can be classified into two main categories: flat spectrum radio quasars and BL Lac objects. Empirically, the distinction between these two classes is based on emission features present in their optical spectra (Stickel et al. 1991). The former class shows strong and broad emission lines, typical of normal quasars, while the latter has almost featureless spectra (i.e. with emission lines of equivalent widths less than 5 Å). Hereinafter we will adopt the nomenclature established by Roma-BZCat (Massaro et al. 2015a), where flat spectrum radio quasars are labelled as BZQs and BL Lac objects as BZBs.

Blazars are the dominant class of active galaxies in the gamma-ray sky (Hartman et al. 1999; Mattox & Ormes 2002; Massaro et al. 2015d). In particular, ∼40% of all associated and classified γ-ray sources detected by the *Fermi* Large Area Telescope (*Fermi*-LAT) 4-year Point Source Catalog (3FGL) belong to this class (Acero et al. 2015). In the last decade, follow-up spectroscopic campaigns (see e.g. Massaro et al. 2014; Álvarez Crespo et al. 2016a,c; Peña-Herazo et al. 2017b; Marchesini et al. 2019b) confirmed that most of the sources classified as "Blazar Candidates of Uncertain type" (BCUs), introduced in the 3FGL catalog, are indeed blazars of the BL Lac type (Massaro et al. 2016; Álvarez Crespo et al. 2016b). The same situation occurs in the preliminary version of the latest release of *Fermi*

catalog[1] (Peña-Herazo et al. 2019). Moreover, follow-up campaigns of unassociated/unidentified γ-ray sources (UGSs) have also shown that a large fraction of them appear to be associated with blazars (Paggi et al. 2014; Massaro et al. 2015c; Landoni et al. 2015; Ricci et al. 2015).

The spectral energy distribution (SED) of blazars shows two components: the lower energy one peaking between infrared and X-rays, and the high energy one peaking between hard X-rays and the γ-ray band. The lower energy component is attributed to synchrotron emission arising from electrons accelerated in their jets, while the high energy component due to the inverse Compton (IC) process (see e.g., Ghisellini et al. 1985; Maraschi et al. 1992; Massaro et al. 2006; Tramacere et al. 2007; Finke et al. 2008; Paggi et al. 2009a; Tramacere et al. 2011, for recent analyses). In particular, for BZBs, the two emission processes are strictly connected, since seed photons for the IC emission are emitted by electrons via synchrotron radiation (i.e. Synchrotron Self-Compton, or SSC, scenario).

Two different sub-classes were originally defined for BZBs distinguishing them on the basis of the on the ratio of their radio to X-ray flux (Maselli et al. 2010): low energy peaked BL Lacs (i.e., LBLs) and high energy peaked ones (i.e., HBLs). This ratio is defined as $\Phi_{\rm XR} = 10^{-3}\,\frac{\rm F_X}{\rm S_{1.4}\Delta\nu}$, where $\rm F_{SX}$ is the X-ray flux from the ROSAT (short for *Röntgensatellit*) survey (Voges et al. 1999) in the 0.1 to 2 keV band, $\rm S_{1.4}\Delta\nu$ is the radio flux density at 1.4 GHz multiplied by the band frequency width $\Delta\nu$. Thus, values of $\Phi_{\rm XR}$ greater than 1 point towards an HBL classification, while values lower than 1 towards an LBL type of source. This corresponds to the limit $\frac{\rm F_X}{\rm S_{1.4}} = 1.0 \times 10^{-11}$.

A strong link between gamma-ray and radio emission in blazars, known as the *gamma-to-radio-connection* (Stecker et al. 1993; Taylor et al. 2007; Bloom 2008; Ghirlanda et al. 2011), was discovered soon after the launch of the Energetic Gamma Ray Experiment Telescope (EGRET) onboard the Compton Gamma-ray satellite (Fichtel et al. 1993). This link was later strengthened thanks to the *Fermi* observations (Mahony et al. 2010; Ackermann et al. 2011; Ghirlanda et al. 2011; Cutini et al. 2014; Lico et al. 2014).

Moreover, combining γ-ray and mid-infrared observations, the latter collected with the Wide-field Infrared Survey Explorer (WISE; Wright et al. 2010), a tight connection between their emissions in these two bands have been also discovered (Massaro et al. 2011a, 2012a; D'Abrusco et al. 2013; Massaro & D'Abrusco 2016). In particular the γ-ray – infrared connection is strongly related not only to the blazar power, but also to their spectral shapes in the two different energy ranges; this is expected given the theoretical interpretation of their SED.

Both these connections strongly fostered follow up campaigns to search for blazar-like counterparts of UGSs, as for example in the radio band (Massaro et al. 2013a; Nori et al. 2014; Lico et al. 2014; Giroletti et al. 2016) and/or applying statistical procedures to find them in the WISE catalogs (D'Abrusco et al. 2013; Massaro et al. 2013b; D'Abrusco et al. 2014; D'Abrusco et al. 2019). On the other hand, X-ray follow up observations have been also carried out to search for blazar-like counterparts of UGSs (e.g., Mirabal 2009; Kataoka et al. 2012; Stroh & Falcone 2013; Paggi et al. 2013; Masetti et al. 2013; Landi et al. 2015; Paiano et al. 2017), even if not supported by any firmly established observational link/connection between X-ray and γ-ray emission of blazars.

Given the SSC scenario underlying the interpretation of BL Lac SEDs, since emission of the low and high energy components are related to the same particle distribution, thus a link between X-ray and γ-ray emission could be expected. This is the main aim of the analysis presented here, focusing on BZBs for which the γ-ray emission should be not significantly contaminated by inverse Compton radiation of seed photons arising from regions outside the jet (Sikora et al. 2013).

We aim to determine which is the fraction of γ-ray blazars with an X-ray counterpart with respect to their γ-ray flux, and if their γ-ray emission (i.e., flux and/or spectral shape) correlates with the X-ray one as occurs in radio and in the mid-IR bands. Our investigation will provide the necessary scientific background to support and justify ongoing (Stroh & Falcone 2013) and future X-ray follow-up campaigns of *Fermi* UGSs. A detailed study of the general behaviour of BZBs in the X-ray band is crucial to improve selection of BZB candidates within a UGS sample. Our search for an X-ray – γ-ray connection is also supported by the fact that HBLs detected at TeV energies (e.g., Piner & Edwards 2014, 2018) are generally among the brightest X-ray sources in the extragalactic sky and their X-ray emission is also linked to the mid-IR one (Massaro et al. 2013e).

To carry out our investigation we analyse observations from the X-ray Telescope (XRT) onboard the Neil Gehrels *Swift* Observatory, performed before mid December 2018, of γ-ray BZBs observed by Fermi. We made this choice since the ROSAT survey is relatively shallow. Only ~60% percent of all known *Fermi* blazars are listed in the ROSAT survey catalog (Voges et al. 1999). Nevertheless *Swift* performs an X-ray follow-up campaign of *Fermi* UGSs[2] (Falcone 2013; Stroh & Falcone 2013; Falcone et al. 2014), thus having an extensive database available.

This paper is organized as follows. In §2 we present sample selection criteria, while in §3 we describe Swift/XRT data reduction procedures. §4 is devoted to results of our analysis, and in §5 we describe a possible interpretation of our results within the SSC framework. Finally, §6 is dedicated to a brief summary and our main conclusions.

Unless stated otherwise, and throughout the whole paper, we adopted cgs units and a flat cosmology with $H_0 = 72\,\rm km\,s^{-1}\,Mpc^{-1}$, and $\Omega_\Lambda = 0.74$ (Dunkley et al. 2009). Spectral indices α were defined so that flux density $\rm S_\nu \propto \nu^{-\alpha}$, considering $\alpha < 0.5$ as *flat spectra*. The AllWISE magnitudes in the [3.4]μm, [4.6]μm, and [12]μm nominal filters are in the Vega system, and are not corrected for Galactic extinction, since this correction is negligible for Galactic latitudes $|b| > 10°$ (see e.g. D'Abrusco et al. 2013).

2. Sample selection

To assess the existence of a connection between the X-ray emission and the γ-ray one in BZBs, we started by selecting all known *Fermi* BZBs listed in the "clean" sample of the Third Catalog of Active Galactic Nuclei detected by the *Fermi*-LAT (Ackermann et al. 2015, 3LAC), considering only those belonging to the fifth release of Roma-BZCat (Massaro et al. 2015a). At this selection step our sample lists 580 sources out of the original 1151. All BZBs in BZCat have a counterpart in at least one of the major radio surveys (White et al. 1997; Condon et al. 1998; Mauch et al. 2003), and all selected ones are uniquely associated to γ-ray sources in the 3FGL catalog.

We only included in our sample *Swift*/XRT observations performed in photon counting (PC) mode, which lied within a circular region of 6 arcmin angular separation around the BZBs γ-ray centroid positions (431 sources). Our choice of 6 arcmin

[1] https://arxiv.org/abs/1902.10045

[2] https://www.*Swift*.psu.edu/unassociated/

corresponds to the average semimajor axis of the positional uncertainty ellipse of gamma-ray sources listed in the 3FGL (Acero et al. 2015). We chose only those sources for which the total exposure time ranged between 1 and 20 ks, since those with cumulative exposure times longer than 20 ks are generally pointed as follow up observations of flaring states and are not snapshot observations, a similar criterion adopted by Mao et al. (2016).

The *Swift* X-ray campaign of UGSs is performed with nominal 5 ks exposure time (Stroh & Falcone 2013), implying that results achieved on our selected sample are suitable to carry out a future investigation of UGSs observed with Swift/XRT (Marchesini et al. 2019, in prep.). Most of the observed fields have 5 ks exposure time with 6.7 ks being the average of our sample.

3. Swift/XRT Data Reduction and Analysis

3.1. Data processing

We adopted the same data reduction procedure described in Massaro et al. (2008b,a); Paggi et al. (2013); Massaro et al. (2011d, 2012b). Here we report the basic details highlighting differences and improvements with respect to our previous analyses.

Raw SWIFT/XRT data were download and reduced to obtain clean event files with the standard procedures, using the XRTPIPELINE task which is part of the *Swift* X-Ray Telescope Data Analysis Software (XRTDAS, Capalbi et al. 2005), and the High Energy Astrophysics Science Archive Research Center (HEASARC) calibration database (CALDB) version x20180710. In particular, using XSELECT we excluded time intervals with count rate exceeding 40 counts per second, and time intervals where the CCD temperature exceeds -50°C in regions located at the CCD edge (D'Elia et al. 2013).

Clean event files were merged using the XSELECT task, while corresponding exposure maps were merged with XIMAGE software. Figure 1 shows a merged image obtained for the XRT field associated to 5BZB J2005+7752, as an example of the final product obtained with our code.

3.2. Source detection & photometry

A first detection run was performed over merged event files using the DET algorithm in XIMAGE, to obtain pixel positions for every detection with signal-to-noise ratios (S/N) larger than 3. Given the relatively low exposure times chosen to carry out our investigation, we focused on a photometric analysis.

Then we run the SOSTA task available within the XIMAGE package on the pixel positions obtained from DET. In particular, SOSTA takes into account the local background for each source to claim a detection, thus achieving a more precise photometry than the DET algorithm. This was carried out on merged event files for the full 0.5-10 keV band, and also for the soft (0.5-2 keV) and hard (2-10 keV) bands. Sources detected with SOSTA had all S/N between 3 and 25.

We compared the resulting X-ray sources with those listed in the *Swift*-XRT point source (1SXPS) catalog (Evans et al. 2014). Our procedure differs from that of 1SXPS in i) the choice of the S/N threshold applied to claim a detection, which is S/N>1.6, ii) the total number of Swift/XRT observations processed (1SXPS used those up to October 2012 while we reduced those up to December 2018), and iii) the choice of background regions (whose shape and size depend on the S/N of the source in 1SXPS). However, we found that our results are in agreement with the 1SXPS catalog, within differences of a few percent (i.e., less than 5%) mainly due to reasons previously highlighted.

Thus, we obtained positions, counts, and countrates for all sources. We flagged sources with full-band countrates higher than 0.5 photons per second, indicating the presence of pile-up. These are 13 sources, all of them with mild pile-up (i.e. with countrates less than 1 photon per second). We then derived the hardness ratio (HR_X) for each source, and full band X-ray fluxes (F_X). The hardness ratio was computed as $(H-S)/(H+S)$, where H are counts in the *hard* band (2 to 10 keV) and S those in the *soft* band (0.5 to 2 keV), respectively. We verified that using counts or countrates to obtain HR_X is equivalent, because the exposure map is not energy dependent in the 0.5-10 keV band. Fluxes were obtained for each source using PIMMS (Mukai 1993), assuming a power-law with a photon index of 2.0 and values of the Galactic column density values obtained from the LAB Survey of Galactic HI (Kalberla et al. 2005). The choice of the photon index affects the estimate of the X-ray flux by a factor of less than a few percent (Massaro et al. 2011b, 2012c). In Table 1, we report the X-ray data and information available thanks to crossmatches performed with multifrequency archives (see Section 4.1 for details). In column 1 we report the BZCat name, in columns 2 to 4 the total counts and their error for the soft (0.5-2.0 keV), hard (2.0-10 keV), and total (0.5-10 keV) bands, in columns 5 to 10 the AllWISE magnitudes and their errors, and in column 11 the X-ray to radio flux ratio, respectively.

4. Results

4.1. X-ray counterparts of γ-ray BL Lac objects

In total, we found 1362 X-ray sources lying for the 351 BZB fields reduced and analyzed.

In Figure 2 we show the distribution of total exposure times of our final sample, of all observed fields, considering those with at least one X-ray detection and those with no X-ray sources above a S/N of 3, separately. In particular, there are 14 BZBs fields within which no XRT counterpart has been found. All these sources were observed for a total exposure time less than 2.4 ks, with two exceptions: 5BZB J1458+3720 (5.3 ks) and 5BZB J0434-2342 (6.8 ks). The former does not show any detection in the XRT merged observation, while the latter shows two X-ray sources lying at more than 6 arcmin from the BZB position. There is, however, a marginal detection with a S/N of 2.8 coincident with the BZB position, which is also detected in the 1SXPS catalog with a S/N of 1.9. Both were discarded due to the absence of a detection above the S/N threshold of 3. Thus the lack of X-ray counterparts for these 14 cases is mainly imputable to our choice of the S/N threshold combined with low exposure time.

The following cuts were also performed *a posteriori*:

1. Spurious X-ray detections due to artifacts and bad pixels or bad columns were discarded.
2. X-ray sources detected close ((i.e., less than 8 arcsec) to a bright source were discarded as artifact of the detection algorithm, with the only exception of that with the highest S/N.
3. Sources that were clearly extended with respect to the XRT 90% PSF (23 arcsec, Moretti et al. 2004) were discarded.
4. Sources not coincident with the BZB position (i.e., out of 5.5 arcsec) and with negative counts on either soft and hard band (defined in Sec. 3.2) were discarded.
5. 5BZB J1104+3812 (a.k.a. Mrk 421), that presented severe pile up contamination, was also discarded. Mrk 421 has been thoroughly studied both in γ-rays and X-rays (e.g. Brinkmann et al. 2005; Isobe et al. 2010; Banerjee et al. 2019; Hervet et al. 2019, and references therein).

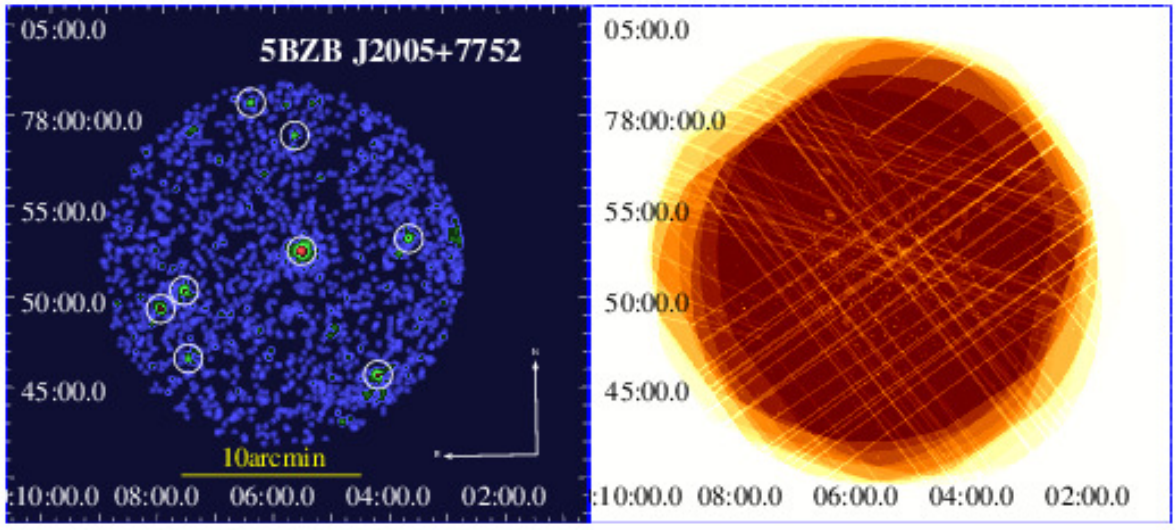

Fig. 1. The X-ray image in the 0.5-10 keV energy range obtained merging all XRT observation within 6 arcmin measured from the gamma-ray position of 5BZB J2005+7752 (left panel) and its corresponding merged exposure map (right panel). The bright source in the center is the X-ray counterpart of the BZB, marked with the white circle as all other background and foreground X-ray sources. This X-ray image has been built merging a total of 5 observations, for a total exposure time of 15.9 ks. The image is also smoothed with a Gaussian kernel of radius 5 pixels.

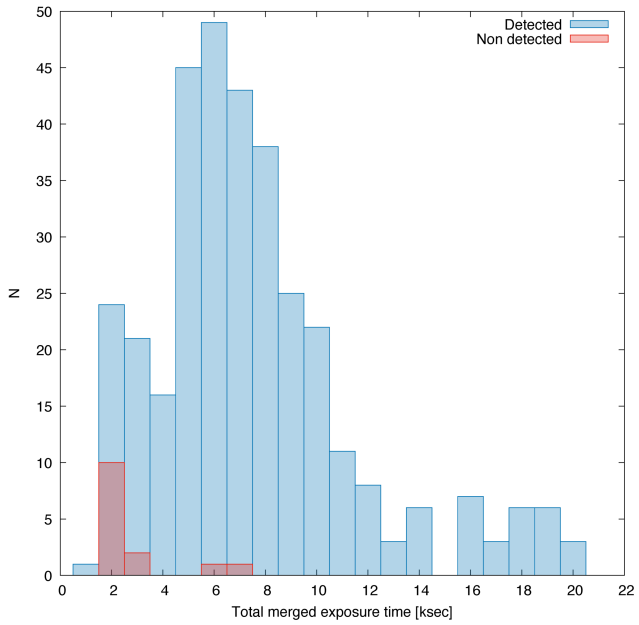

Fig. 2. The distribution of the total exposure time for all selected BZBs. The blue histogram indicates those X-ray merged event files with at least an X-ray source detected with S/N greater than 3, while in red those with no X-ray detection.

6. Two BZBs lying in the same field within the positional uncertainty region of the same *Fermi* source, namely 3FGL J0323.6-0109 (i.e., 5BZB J0323-0111 and 5BZB J0323-0108) were also discarded, due to possible source confusion in γ-rays.

In addition we also crossmatched X-ray positions with AllWISE catalog with a uncertainty radius of 3.3 arcsec, following D'Abrusco et al. (2013). All mid-IR counterparts were correctly associated with the XRT detections with two exceptions: 5BZB J0335-4459 (at 3.8 arcsec) and 5BZB J2131-2515 (at 3.5 arcsec)[3]. Being in any case the closest WISE source and unique matches we kept both BZBs in our sample.

From the 351 Fermi BZBs observed by *Swift*/XRT for 1 to 20 ks, 337 were detected and 14 were not. In addition, three BZBs were discarded due to pile-up or source confusion. Thus, we built a clean sample of 334 BZBs with X-ray and mid-IR counterparts, and a clean sample of 675 background and foreground X-ray sources lying within an angular separation of 6 arcmin from the γ-ray position. The flow chart shown in Figure 3 summarized all our selection steps.

4.2. X-ray properties of γ-ray BL Lac objects

We detected 337 BZBs using XRT data out of the original selected sample of 351 *Fermi* BZBs. This means that 96% of BZB sources listed by *Fermi* show an X-ray counterpart when observed for more than 1ks. This strongly supports the existence of an X-ray – γ-ray connection and certainly motivates X-ray follow up observations at least to the level of γ-ray flux of our current BZB sample to search for UGS counterparts (Massaro et al. 2013c).

In Figure 4 we show the distribution of γ-ray energy flux in the 100 MeV to 100 GeV band for all *Fermi* BZBs in our sample, divided into those for which we found at least one X-ray counterpart and those for which no XRT counterpart was detected. We plotted the γ-ray flux thresholds above which we found at least one X-ray counterpart for 100% ($F_\gamma = 1.7 \times 10^{-11}$ erg cm^{-2} s), 98% ($F_\gamma = 7.0 \times 10^{-12}$ erg cm^{-2} s) and 96% ($F_\gamma = 2.9 \times 10^{-12}$ erg cm^{-2} s) of the sample. We expect that these thresholds can be used to find new BZBs among the Fermi UGSs.

The nominal exposure time used for the UGS XRT follow-up campaign is of 5 ks (Stroh & Falcone 2013). Thus, we verified the fraction of BZBs that could be detected re-scaling the exposure time to this nominal value. We selected only those sources

[3] 5BZBJ 1046-2535 was not included due to light contamination from a nearby star. 5BZB J2108-6637 is the only source for which no WISE counterpart was found.

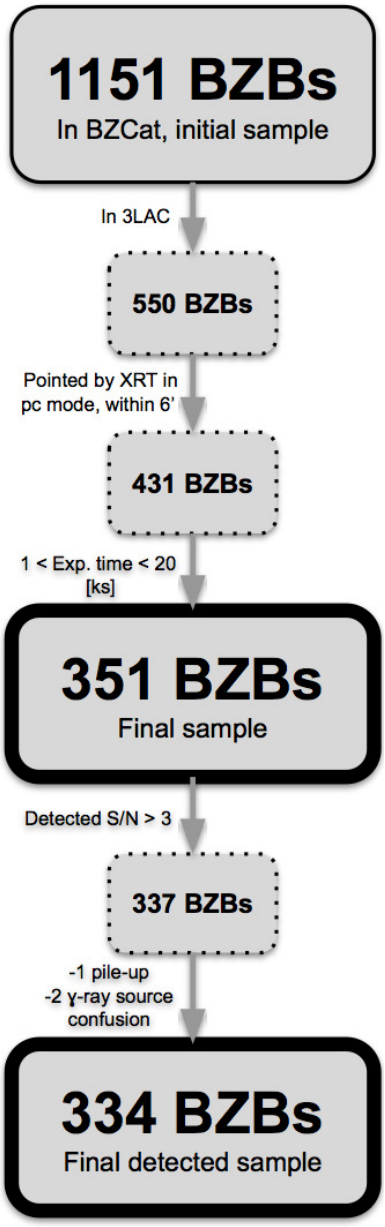

Fig. 3. The flow chart to highlight all steps followed to build our final BZBs sample.

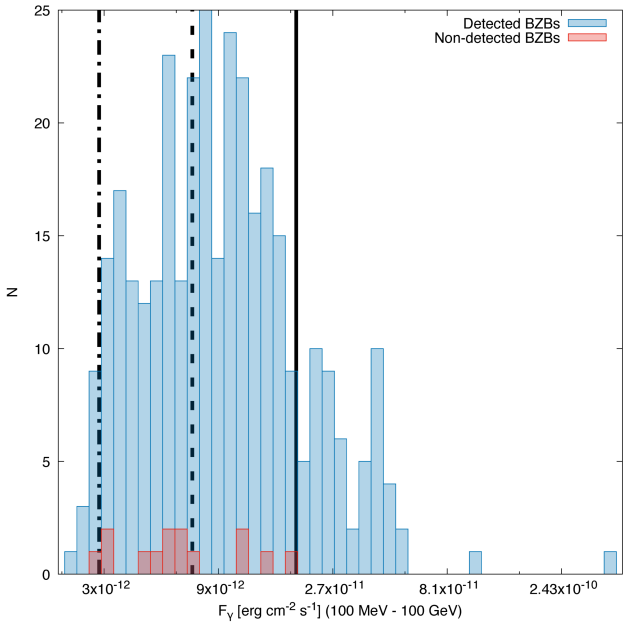

Fig. 4. The distribution of F_γ in the 100 MeV to 100 GeV band for all 351 BZBs in our selected sample. As in Fig. 2 the blue histogram indicates those X-ray merged event file with at least an X-ray source detected with S/N greater than 3 while in red those with no X-ray detection. The solid black line corresponds to the threshold above which 100% of selected BZBs has an X-ray counterpart, while the dashed and dot-dashed black lines mark the 98% and 96%, respectively.

for which the total (merged) exposure time was over 5 ks (222 sources), and then scaled their S/Nassuming a Poisson distribution of observed countrates. We confirm that 98% of our selected sample would still be detected at a S/N ratio greater than 3 with lower (i.e., 5ks) exposure time.

The HBL versus LBL classification was done following Maselli et al. (2010), as mentioned in §1. The 1.4 GHz radio fluxes were taken from BZCat for each source, with the exception of 5BZB J1326-5256 and 5BZB J1604-4441 for which only the flux at 4.85 GHz was available. We assumed that the spectral shape of blazars is flat (radio spectral index equal to zero) at radio frequencies (see e.g. Healey et al. 2007; Massaro et al. 2013a,d), so we considered the 4.85 GHz flux to be equal to that at 1.4 GHz. Since the XRT band (0.5-10 keV) differs from that of ROSAT (0.1-2.4 keV), which is the one originally used for this classification, we compared the use of full-band fluxes adjusted to the ROSAT band assuming a power law. The HBL and LBL classification is the same using either of the X-ray flux estimates. Then we adopted full-band XRT fluxes. In particular, in Table 1 we chose to show the full band XRT to radio flux ratio $F_X/S_{1.4}$ instead of Φ_{XR}, so that the limit between classes is of $F_X/S_{1.4} > 10^{-11}$.

In total, 175 sources out of the total 334 are HBLs, while the remaining 159 are classified as LBLs. As expected, errors in HR_X and F_X for HBL and LBL objects are smaller than for background/foreground objects, as BZBs are generally one order of magnitude brighter (average flux $F_X = 3.9 \times 10^{-12}$ erg cm^{-2} s^{-1}) than background/foreground objects (average flux $F_X = 2.7 \times 10^{-13}$ erg cm^{-2} s^{-1}). On the other hand, HBLs and LBLs have softer X-ray spectra than background/foreground objects, which span all the possible HR_X values. In Figure 5 we show F_X versus HR_X plotted for all detected sources (i.e., BZBs and background/foreground X-ray objects). **BZBs are separated into HBLs and LBLs with a color code indicating their Φ_{XR} value, going from green (HBLs) to orange (LBLs), while sources with $\Phi_{XR} \approx 1$ are in yellow.** The average value for the HR_X is $HR_X = -0.63 \pm 0.09$ for HBLs and $HR_X = -0.46 \pm 0.16$ for LBLs. Sources with $F_X > 2.0 \times 10^{-11}$ erg cm^{-2} s^{-1} (indicated with black solid line) suffer from pile-up. **The HBL and LBL subsamples lie in different regions, as do background/foreground objects. Intermediate sources (i.e. with $\Phi_{XR} \approx 1$) lie in between both regions, as expected. This is also true in all Figures shown from this point on.**

To quantify the separation between each subsample in the F_X–HR_X space, we performed a Kernel Density Estimation (KDE) analysis, in order to estimate density thresholds for each subsample. In Figure 6 we show F_X versus HR_X for background/foreground objects and for BZBs separated into HBLs and LBLs, with isodensity contours obtained from the KDE analysis for each subsample, at 70%, 80% and

Table 1. First 10 rows for the main results of our analysis. In column 1 we report the source name as listed in BZCat, in columns 2 and 3 the total counts and their error for the soft (0.5-2.0 keV) and hard (2.0-10 keV) bands, in column 4 the total band (0.5-10 keV) flux and its uncertainty, in erg cm^{-2} s^{-1} units, in columns 5 to 10 the AllWISE magnitudes and their uncertainties for each source, and in column 11 the X-ray to radio flux ratio. The AllWISE magnitudes W1, W2 and W3 correspond to wavelengths 3.4 μm, 4.6 μm, and 12 μm, respectively. Sources with pile-up are marked with a † next to their name. The complete table is available online.

Source	Soft [photons]	Hard [photons]	Flux [$\times 10^{-12}$erg cm^{-2} s^{-1}]	W1 [mag]	σ_{W1} [mag]	W2 [mag]	σ_{W2} [mag]	W3 [mag]	σ_{W3} [mag]	$F_X/S_{1.4}$ [$\times 10^{-12}$]
5BZB J0001-0746	22.3 ± 5.5	11.4 ± 3.9	0.3 ± 0.05	12.68	0.01	11.76	0.01	9.17	0.04	1.4
5BZB J0004-1148	55.7 ± 8.2	13.9 ± 4.3	0.5 ± 0.06	14.10	0.02	13.12	0.04	10.4	0.1	1.0
5BZB J0008-2339	533.7 ± 26.0	122.2 ± 13.0	5.5 ± 0.2	13.75	0.02	13.29	0.03	11.3	0.2	150
5BZB J0009+0628	69.6 ± 10.0	23.4 ± 6.1	0.5 ± 0.06	12.97	0.01	12.04	0.02	9.36	0.04	2.1
5BZB J0009+5030	44.6 ± 7.5	9.1 ± 3.4	0.4 ± 0.05	12.97	0.02	12.44	0.02	10.37	0.08	29
5BZB J0014-5022	1051.0 ± 37.0	293.4 ± 19.0	7.6 ± 0.2	14.74	0.03	14.6	0.1	11.9	-	590
5BZB J0019+2021	15.9 ± 4.7	5.8 ± 2.8	0.2 ± 0.05	14.44	0.04	13.39	0.06	10.4	0.1	0.2
5BZB J0019-8152	91.3 ± 11.0	9.8 ± 4.0	0.6 ± 0.06	12.209	0.007	11.331	0.007	8.98	0.02	6.8
5BZB J0021-2550	35.9 ± 6.9	4.9 ± 2.8	0.2 ± 0.03	13.38	0.02	12.54	0.02	10.24	0.08	3.0
5BZB J0022+0608	67.3 ± 8.9	19.8 ± 5.2	0.4 ± 0.05	12.92	0.02	11.88	0.01	9.08	0.04	1.2

90% level. Although the subsamples overlap with each other, when considering a 90% density level the overlap is minimum. Moreover, HBLs lie in a very distinct region at all density levels.

From Figures 5 and 6, it follows that the LBL and HBL classification following Maselli et al. (2010) coincides with our results obtained through a KDE analysis, with intermediate-type objects populating the overlapping isodensity area between both classes.

In Figure 7, we also show the distribution of the angular separation between the X-ray and the γ-ray positions in the same field. X-ray detected BZBs on average appear to be closer to their γ-ray counterpart than background X-ray sources in the examined fields. This is confirmed through a Kolmogorov-Smirnov test, which yields a negligible chance coincidence probability, or p-chance p. This implies a low contamination by background/foreground sources.

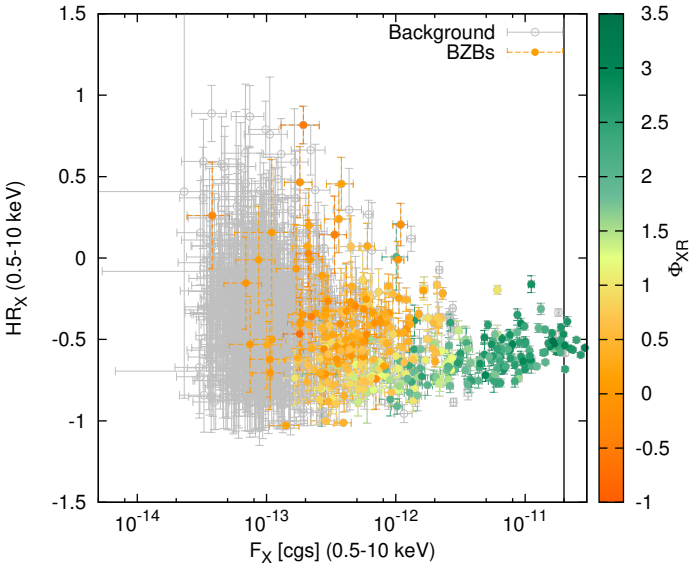

Fig. 5. F_X in the 0.5-10 keV band versus HR_X for all BZBs in the selected sample. Background/foreground X-ray sources are marked in grey while BZB classified as HBL and those as LBL are marked in green and orange, respectively. The solid black line separates BZBs with pile-up, which show $F_X > 2.0 \times 10^{-11}$ erg cm^{-2} s^{-1}.

In Figure 8 we report F_X versus the WISE mid-IR magnitude at 12 μm (in the upper panel), and versus the gamma-ray energy flux in the 100 MeV - 100 GeV band, taken from the 3FGL catalog (in the upper panel). The 12 μm magnitude is the least affected by Galactic extinction, while still more sensitive than the W4 magnitude at 22 μm (D'Abrusco et al. 2012). No neat trend is visible in either panel of Figure 8. This is expected, since while γ-rays are dominated by the IC SED component, X-rays are due to synchrotron emission in HBLs but could be a combination of both synchrotron and IC components in LBLs (Bondi et al. 2001; Massaro et al. 2008a). There is no neat trend visible between F_X and the γ-ray energy flux. However, we highlight that since 96% γ-ray BZBs have a counterpart in the X-rays, this provides a direct link between the BZB emission in these two energy ranges. We recall that HBLs are on average

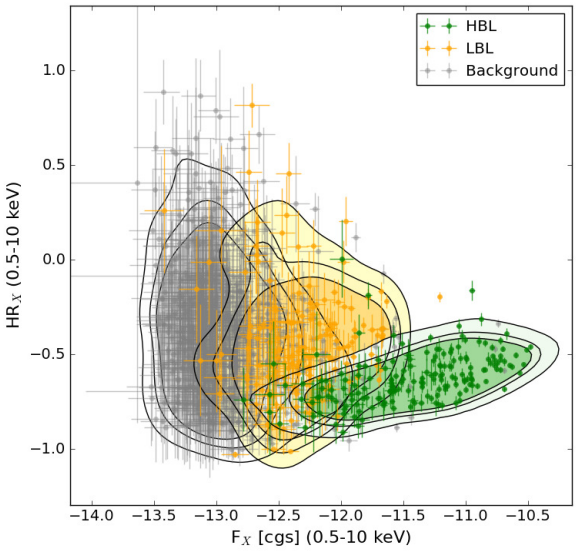

Fig. 6. F_X **in the 0.5-10 keV band versus** HR_X **for all BZBs in the selected sample, same as in Figure 5. 70%, 80% and 90% isodensity contours as obtained from a KDE analysis are shown for Background/Foreground sources in grey, HBLs in green and LBLs in orange.**

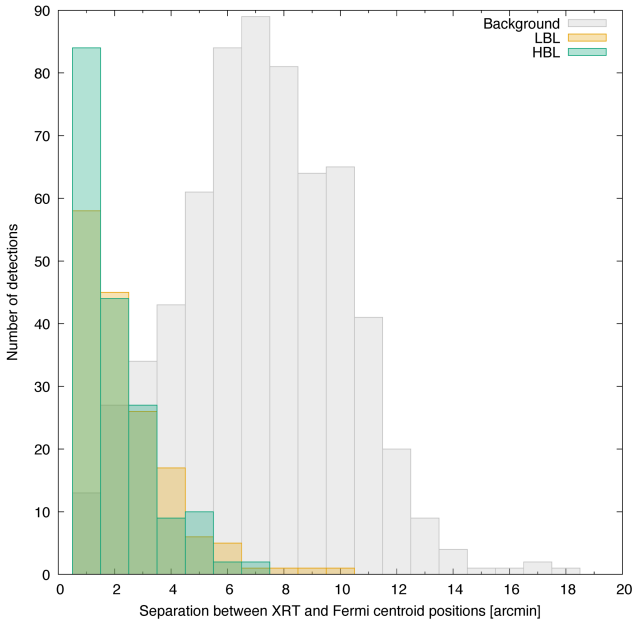

Fig. 7. Angular separation between the X-ray and the γ-ray position for all BZBs, in arcminutes. As in Fig. 5, BZBs classified as HBLs and LBLs are shown in green and orange, respectively, while background/foreground X-ray sources are in grey.

an order of magnitude brighter in X-rays than LBLs. The average F_X value is $(4.5 \pm 3.3) \times 10^{-12}$ erg cm^{-2} s^{-1} for HBLs, and $(4.5 \pm 1.9) \times 10^{-13}$ erg cm^{-2} s^{-1} for LBLs. On the other hand, LBLs are an average of 0.6 magnitudes brighter in mid-IR than HBLs.

The distinction between HBLs and LBLs becomes clearer when comparing their X-ray, γ-ray and mid infrared spectral shapes. In Figure 9, we show F_X versus the mid-IR color computed with WISE magnitudes at 4.6μm and 12μm (upper panel)

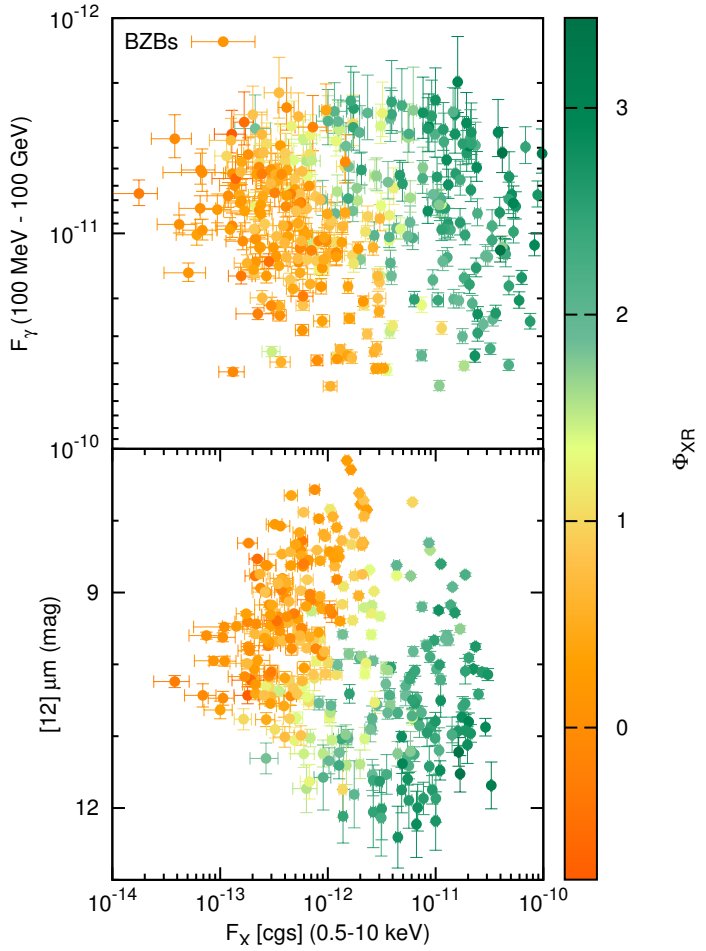

Fig. 8. Lower panel: F_X in the 0.5-10 keV band versus the WISE magnitude at 12 μm for all selected BZBs. Upper panel: F_X in the 0.5-10 keV band versus the F_γ in the 100 MeV - 100 GeV band, collected from the 3FGL. BL Lac objects classified as HBLs and LBLs are shown in green and orange, respectively

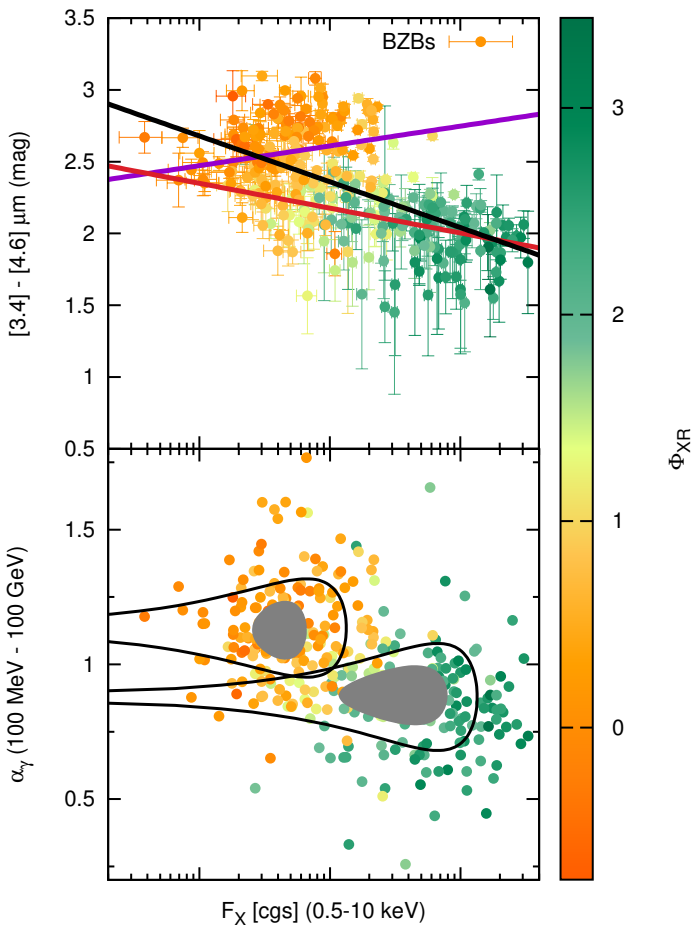

Fig. 9. Upper panel: F_X in the 0.5-10 keV band versus the [4.6]-[12] μm mid-IR color. Selected BZBs are classified as HBLs and LBLs marked in green and orange, respectively. Dashed lines indicates regression lines for LBLs (purple), HBLs (red) and the whole sample (black). Lower panel: F_X in the 0.5-10 keV band versus the α_γ as reported in the 3FGL. Solid black lines mark the area within one standard deviation centered on the mean, while solid grey area indicates that computed with the median absolute deviation centered on the median value.

and versus the gamma-ray spectral index reported in the 3FGL (lower panel). It can be seen that HBLs are brighter in X-rays and harder in γ-rays than LBLs (Ghisellini et al. 2010, 2017). In the lower panel of Figure 9 we also plot the average and median values of these parameters for both samples, together with their standard deviation and median absolute deviation, to highlight the neat distinction between the two sub-classes. Although we could not establish a neat trend between fluxes or spectral shapes of BZBs in the X-ray and the γ-ray band, we proved that there is a link between emission in these two energy ranges given by the Fermi BZB high detection rate in the Swift/XRT observations analyzed here.

This is different from what was discovered between radio, mid-infrared and gamma-ray emission for this class of AGNs, but it is crucial to support on going and future X-ray campaign searching for blazars within sample of UGSs as well as spectroscopic follow up observations of X-ray sources lying within the positional uncertainty region of unassociated Fermi sources.

The previous distinction improves significantly when using the mid-IR color, mainly because it marks better the difference in the synchrotron component between HBLs and LBLs. Indeed, we found a correlation between F_X and the [4.6]-[12]μm WISE color index, with a slope of ~ -0.32 and a p-chance of $p < 1 \times 10^{-7}$, for the whole sample of BZBs (plotted as a black line in Figure 9). This is due to the shifting of the whole Synchrotron component towards higher energies, since X-rays and IR trace two different sides of the Synchrotron peak. The trend is clearer for HBLs than for LBLs possibly due to the contribution of the IC component in the SEDs of the latter subclass. The p-chance of both correlations are $p \sim 3.7 \times 10^{-7}$ for HBLs (plotted in red) and $p \sim 0.019$ for LBLs (plotted in purple), respectively, indicating that the second is not statistically significant. In almost all previous WISE and X-ray combined investigations (see e.g., Maselli et al. 2013), the lack of uniform X-ray datasets did not allow to compare the behaviour of HBLs and LBLs, as done here.

In Figure 10 we show HR_X versus the mid-IR color (upper panel), and versus the gamma-ray spectral index (lower panel), respectively. We note that HBLs tend to cover a small range of X-ray hardness ratios, appearing to have softer X-ray spectra than LBLs. The average value for the HR_X is -0.63 ± 0.09 for HBLs and -0.46 ± 0.16 for LBLs. The opposite occurs for the γ-ray spectral index and mid-IR colors, where HBLs show a wider range of values with respect to LBLs.

Finally, for 77 BZBs a redshift estimate was available in Roma-BZCat allowing us to compute their X-ray luminosities (L_X), as shown in Figure 11. HBLs tend to be more luminous

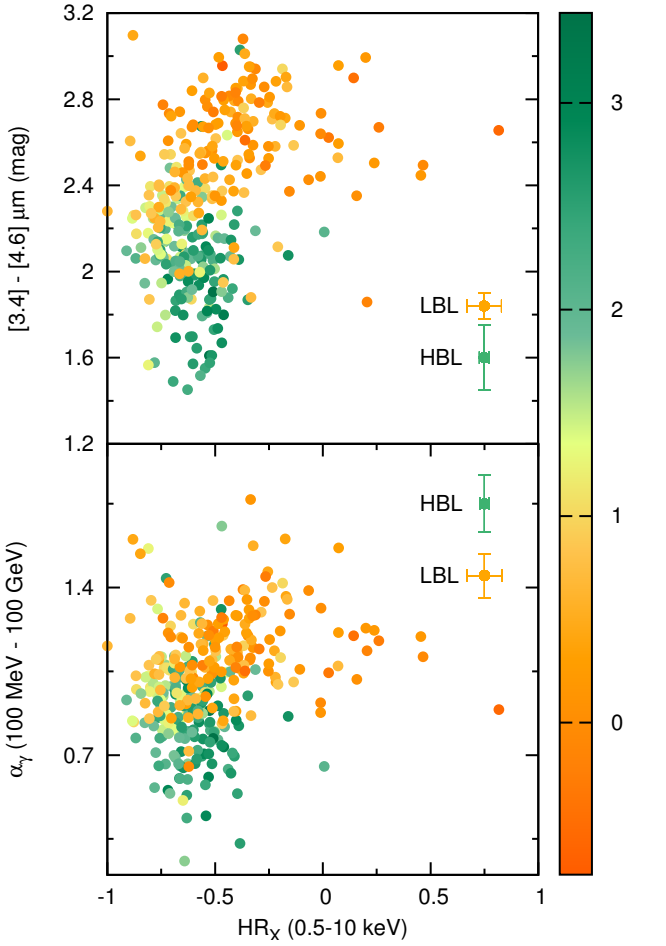

Fig. 10. Spectral shape comparison for all the BZBs in our sample. LBLs are shown in orange while HBLs in green. Upper panel: HR_X in the 0.5-10 keV band versus the [4.6]-[12] μm mid-IR color. Lower panel: HR_X in the 0.5-10 keV band versus α_γ. In both panels, average uncertainties on the parameters are shown as crosses in the top right corner.

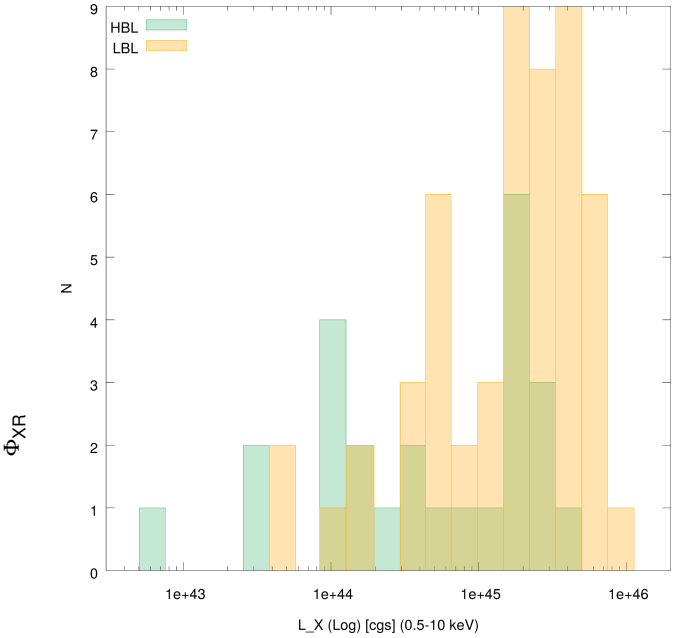

Fig. 11. The distribution of L_X in the 0.5-10 keV band, for the subsample of 77 BZBs with a well determined redshift estimate reported in the Roma-BZCat (Massaro et al. 2015a). As in previous figures, LBLs are in orange while HBLs in green.

than LBLs in the X-ray band. This could be due to the redshift difference, being on average 0.283 for HBLs and 0.443 for LBLs. However, we also noticed that their corresponding gamma-ray luminosities (L_γ) are indeed quite similar for the same sample.

5. Theoretical interpretation

The theoretical connection between synchrotron and IC processes in the SSC scenario has been already extensively investigated (see e.g., Dermer 1995; Bloom & Marscher 1996; Mastichiadis & Kirk 1997; Dermer & Schlickeiser 2002; Massaro et al. 2006; Tramacere et al. 2011, and references therein). However, possible observable connections between X-ray and γ-ray emissions in BZBs are not yet fully exploited, certainly not on a statistical sample as the one analyzed here.

As previously stated, while carrying out this investigation we found that HBLs tend to be brighter in the X-rays than LBLs and cover a wider range of fluxes. On the other hand, LBLs cover a wide range of HR_X, being generally harder than HBLs in the X-rays. These results suggest that on average HBLs do not vary significantly their X-ray spectral shape but only their total integrated power, while the opposite occurs for LBLs.

According to the SSC scenario, we could interpret this as follows. For LBLs a decrease in synchrotron emission in the X-rays could be balanced by an increase of the IC component. This implies a certain balance in the total X-ray flux, but a noticeable change in the spectral shape (i.e. X-ray hardness ratio HR_X). On the other hand, the fact that for HBLs, HR_X is restricted to a narrow range of values implies that the position of the synchrotron peak remains constant on average, and that we are only observing the high energy tail of their synchrotron component in X-rays.

We expect that the HBL behavior in X-rays is consistent with the theoretical scenario proposed in Massaro et al. (2011c) on the basis of the acceleration mechanism proposed by Cavaliere & Morrison (1980). Thus, assuming that the beaming factor of HBL jets does not vary significantly, as the total number of emitting particles, and following Paggi et al. (2009b), we state that the frequency of the synchrotron peak scales as $\nu_s \propto \gamma_{3p}^2 B$, where B is the average magnetic field in the emission region and γ_{3p} the peak of the $\gamma\, n(\gamma)$, with $n(\gamma)$ the particle energy distribution (see Tramacere et al. 2007, 2011, for details). For HBLs, ν_s remains constant on average, implying that $\gamma_{3p}^2 B = \text{const}$. Assuming that the IC emission occurs in Thomson regime, we expect that the SED peak frequency of the high energy component scales as $\nu_{ic} \propto \gamma_{3p}\, \nu_s$, thus as γ_{3p}^2 under the circumstances previously described. On the other hand the peak height of the IC component being in general proportional to $\gamma_{3p}^4\, B^2$ does not show significant changes, if particle energy distribution and magnetic field are the main driver of spectral variations (Paggi et al. 2011).

According to Blandford & Znajek (1977) and Cavaliere & D'Elia (2002), the BZB luminosity should be limited by the Blandford-Znajek (BZ) limit (Ghosh & Abramowicz 1997; Tchekhovskoy et al. 2009), defined as $L_{BZ} \leq 8 \times 10^{45} \times \left(\frac{M_{BH}}{10^9\, M_{Sun}}\right)$ erg s^{-1}, where M_{BH} is the central black hole mass, and M_{Sun} the mass of the Sun. This condition applies only if the output can be ascribed solely to the black hole (i.e. in "dry"

sources), which is an useful benchmark to analyse whether accretion is negligible or not in BZBs (Paggi et al. 2009a).

There is, however, evidence that BZBs could be emitting more than what can be described only within this benchmark (see, for example, Tavecchio & Ghisellini 2016). In presence of significant current accretion, we expect the jet launched from the central black hole to be more powerful (Ghisellini et al. 2014), and thus yielding larger observed luminosities, ultimately exceeding the BZ limit, that instead applies to sources only powered by rotation.

For our sample we found 27 black hole mass estimates, measured with different methods as reported by Woo et al. (2005); Plotkin et al. (2011); León-Tavares et al. (2011); Sbarrato et al. (2012); Shaw et al. (2012); Xiong & Zhang (2014) and Ghisellini & Tavecchio (2015). We used them to compute the ratio of the sum of $L_X + L_\gamma$ to the BZ Luminosity limit. L_X was computed from our data in the 0.5-10 keV band, while L_γ was obtained in the 100 MeV to 100 GeV band as listed in 3FGL. We adopted $L_X + L_\gamma$ as an estimate of the bolometric luminosity, since at least one of them is close to the SED peak. Thus, we expect the ratio to be below 1 if the BZ limit is applicable. In Figure 12 we plotted this ratio versus the position of the rest-frame synchrotron peak taken from the 3FGL catalog.

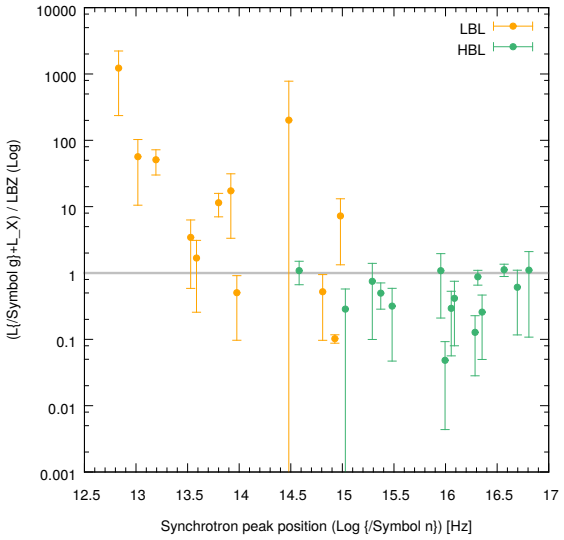

Fig. 12. Synchrotron peak frequency versus the ratio between the estimate of the bolometric luminosity and the Blandford-Znajek luminosity, computed as reported in Section 5. As in previous figures. LBLs are in orange while HBLs in green. The grey dashed line indicates a luminosity ratio of 1, below which "dry" BZBs should lie.

It is clear that all HBLs are still below the BZ limit, which is expected since their are the less bolometrically luminous kind of blazar (Sambruna et al. 1996).

In the LBL case, however, eight out of twelve are above the BZ limit. Although the subsample is small, this is a hint that the BZ benchmark does not apply cleanly to the LBL scenario, as it does for HBLs.

A possible explanation for this discrepancy between the BZ benchmark and the observed LBL luminosities could be that these eight sources are probably not 'dry' sources as HBLs. Thus their broad-band emission is contaminated by IC scattering of seed photons arising from surrounding gas and/or the accretion disk (Abdo et al. 2015; Arsioli & Chang 2018). This is also consistent with the fact that LBLs are more similar to BZQs, and in these cases the accretion component is important. In particular, for all these cases L_γ is more than one order of magnitude higher than the X-ray luminosity, which is a strong indication that emission in these sources is strongly affected by an External Compton process (Arsioli & Chang 2018).

6. Summary and Conclusions

In this work we aimed at characterizing the X-ray properties of *Fermi* BZBs, searching for a possible X-ray – γ-ray connection that could motivate follow up X-ray observations to discover new blazar-like counterparts of UGSs (Stroh & Falcone 2013; Paggi et al. 2013; Massaro et al. 2015b). To achieve our goal, we built a sample of 351 BZBs listed by *Fermi* that were observed by the *Swift*/XRT telescope, in photon counting mode, with exposure times between 1 and 20 ks, and collected up to December 2018.

1. 96% (337) of the 351 *Fermi* BZBs which were observed by XRT for more than 1ks were detected with S/N greater than 3 (mean S/N ratio of 25). We obtained accurate positions, counts, countrates, fluxes, and images for all of them in the soft X-ray band between 0.5 and 10 keV.
2. BZBs are on average brighter in X-rays than other X-ray emitting sources lying outside of the galactic plane ($|b| > 10°$). When classified as HBLs and LBLs, HBLs are generally brighter in X-ray flux and cover a wider range of flux values than LBLs.
3. On the other hand, the spectral shape of LBLs in X-rays is harder and less uniform than that of HBLs. This could be due to a more variable spectral shape in the X-ray band: for HBLs, the X-ray emission is dominated by the synchrotron process, while for LBLs the IC component is non negligible.
4. We proved there is a direct link between the X-ray and γ-ray emission in BZBs, as supported by the high detection rate (96%) of their X-ray counterparts. This rate would remain unchanged even with lower exposure times (5 ks).
5. There is a correlation between F_X and the mid-IR color [4.6]-[12]μm ($p < 1 \times 10^{-7}$). X-ray brighter BZBs are bluer in the mid-IR.
6. For a subsample of 77 sources we obtained redshifts values which allowed us to compute distances and luminosities. We note that HBLs are bolometrically less luminous than LBLs.
7. For 27 sources out of these 77 with a determined redshift, we also looked for central black hole mass values in the literature. All HBLs are below their Blandford-Znajek limit. However, some LBLs exceed this limit. We speculate this indicates that LBLs may be accreting more gas than HBLs, meaning that the 'dry' hypothesis would be valid only in the latter, not in the former.

7. Acknowledgements

E. J. Marchesini would like to thank Dr. Rocío I. Páez and Dr. M. Victoria Reynaldi for useful discussions on this work. This work is supported by the "Departments of Excellence 2018 - 2022" Grant awarded by the Italian Ministry of Education, University and Research (MIUR) (L. 232/2016). This research has made use of resources provided by the Compagnia di San Paolo for the grant awarded on the BLENV project (S1618_L1_MASF_01) and by the Ministry of Education, Universities and Research for the grant MASF_FFABR_17_01. F.M. acknowledges financial contribution from the agreement ASI-INAF n.2017-14-H.0

A.P. acknowledges financial support from the Consorzio Interuniversitario per la fisica Spaziale (CIFS) under the agreement related to the grant MASF_CONTR_FIN_18_02. This research has made use of data obtained from the high- energy Astrophysics Science Archive Research Center (HEASARC) provided by NASA's Goddard Space Flight Center. This work is part of a project that has received funding from the European Union's Horizon 2020 Research and Innovation Programme under the Marie Słodowska-Curie Grant Agreement No. 664931. Part of this work is based on the NVSS (NRAO VLA Sky Survey). The National Radio Astronomy Observatory is operated by Associated Universities, Inc., under contract with the National Science Foundation. The Molonglo Observatory site manager, Duncan Campbell- Wilson, and the staff, Jeff Webb, Michael White, and John Barry, are responsible for the smooth operation of the Molonglo Observatory Synthesis Telescope (MOST) and the day-to-day observing program of SUMSS. SUMSS is dedicated to Michael Large, whose expertise and vision made the project possible. The MOST is operated by the School of Physics with the support of the Australian Research Council and the Science Foundation for Physics within the University of Sydney. This publication makes use of data products from the Wide-field Infrared Survey Explorer, which is a joint project of the University of California, Los Angeles, and the Jet Propulsion Laboratory/California Institute of Technology, funded by the National Aeronautics and Space Administration. TOPCAT[4] (Taylor 2005) and STILTS (Taylor 2006) were used for the preparation and manipulation of the images and the tabular data.

8. Appendix

In this section we include complementary Figures.

In Figure 13 we show the X-ray full-band flux versus the magnitudes at 3.4 and 4.6 μm from the AllWISE catalog, in the upper and lower panel, respectively. These do not differ from the aforementioned results, as seen in Figure 10. In the same way, we show in Figure 14 the comparison between the X-ray full band flux and the color index [3.4]-[4.6], which is comparable to Figure 11. Finally, in Figure 15 we show the X-ray hardness ratio versus the color index [3.4]-[4.6], which follows the same trend discussed in the case of Figure 10.

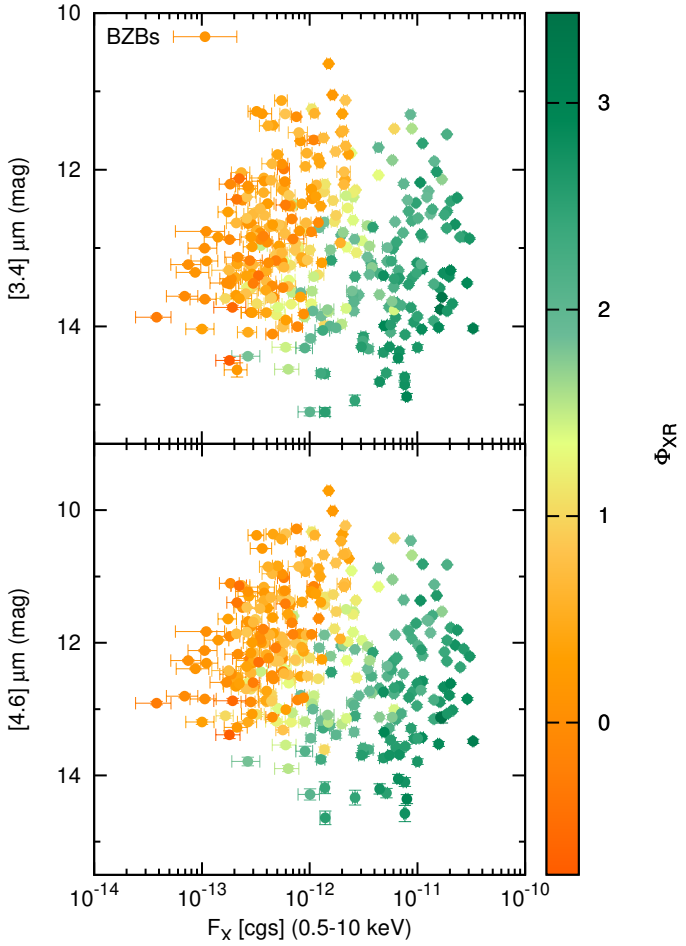

Fig. 13. F_X in the 0.5-10 keV band versus the WISE magnitude estimate at nominal wavelength of 3.4 μm (upper panel) and versus that evaluated at 4.6 μm (lower panel). BZBs classified as LBL are shown in orange while HBLs are marked in green.

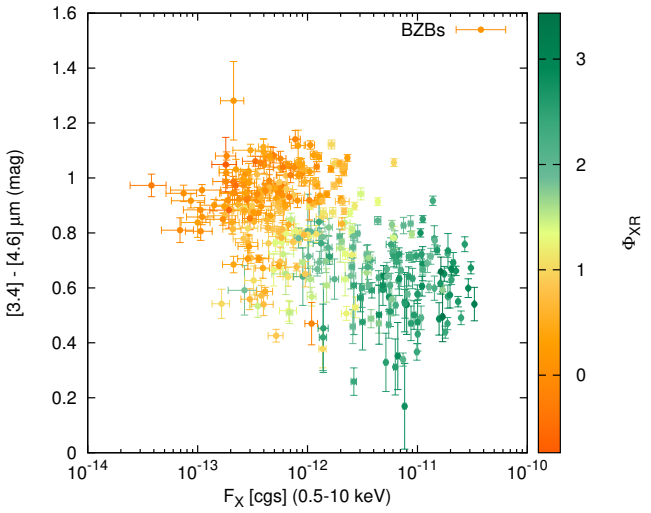

Fig. 14. F_X in the 0.5-10 keV band versus the [3.4]-[4.6] μm mid-IR color.

[4] http://www.star.bris.ac.uk/m bt/topcat/

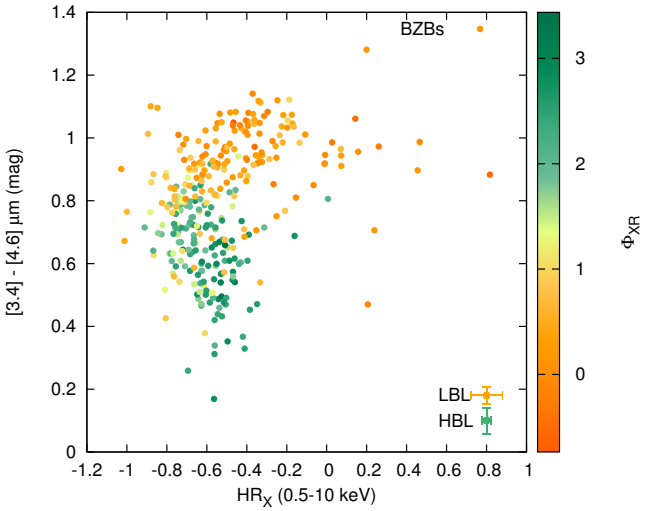

Fig. 15. HR_X in the 0.5-10 keV band versus the [3.4]-[4.6] μm. Average uncertainties on these two parameters are shown as crosses in the bottom right corner.

References

Abdo, A. A., Ackermann, M., Ajello, M., et al. 2015, ApJ, 799, 143
Acero, F., Ackermann, M., Ajello, M., et al. 2015, ApJS, 218, 23
Ackermann, M., Ajello, M., Allafort, A., et al. 2011, ApJ, 741, 30
Ackermann, M., Ajello, M., Atwood, W. B., et al. 2015, ApJ, 810, 14
Aharonian, F., Akhperjanian, A. G., Aye, K.-M., et al. 2005, A&A, 436, L17
Albert, J., Aliu, E., Anderhub, H., et al. 2007, ApJ, 669, 862
Álvarez Crespo, N., Masetti, N., Ricci, F., et al. 2016a, AJ, 151, 32
Álvarez Crespo, N., Massaro, F., D'Abrusco, R., et al. 2016b, Ap&SS, 361, 316
Álvarez Crespo, N., Massaro, F., Milisavljevic, D., et al. 2016c, AJ, 151, 95
Arsioli, B. & Chang, Y. L. 2018, A&A, 616, A63
Banerjee, B., Joshi, M., Majumdar, P., et al. 2019, MNRAS, 487, 845
Blandford, R. D. & Rees, M. J. 1978, in BL Lac Objects, ed. A. M. Wolfe, 328–341
Blandford, R. D. & Znajek, R. L. 1977, MNRAS, 179, 433
Bloom, S. D. 2008, AJ, 136, 1533
Bloom, S. D. & Marscher, A. P. 1996, ApJ, 461, 657
Bondi, M., Marchã, M. J. M., Dallacasa, D., & Stanghellini, C. 2001, MNRAS, 325, 1109
Böttcher, M., Basu, S., Joshi, M., et al. 2007, ApJ, 670, 968
Brinkmann, W., Papadakis, I. E., Raeth, C., Mimica, P., & Haberl, F. 2005, A&A, 443, 397
Bruni, G., Panessa, F., Ghisellini, G., et al. 2018, ApJ, 854, L23
Capalbi, M., Perri, M., Saija, B., & Tamburelli, F. 2005, ASI Science Data Center, 1
Carini, M. T., Miller, H. R., Noble, J. C., & Goodrich, B. D. 1992, AJ, 104, 15
Cavaliere, A. & D'Elia, V. 2002, ApJ, 571, 226
Cavaliere, A. & Morrison, P. 1980, ApJ, 238, L63
Ciaramella, A., Bongardo, C., Aller, H. D., et al. 2004, A&A, 419, 485
Condon, J. J., Cotton, W. D., Greisen, E. W., et al. 1998, AJ, 115, 1693
Cutini, S., Ciprini, S., Orienti, M., et al. 2014, MNRAS, 445, 4316
D'Abrusco, R., Massaro, F., Ajello, M., et al. 2012, ApJ, 748, 68
D'Abrusco, R., Massaro, F., Paggi, A., et al. 2013, ApJS, 206, 12
D'Abrusco, R., Massaro, F., Paggi, A., et al. 2014, ApJS, 215, 14
D'Elia, V., Perri, M., Puccetti, S., et al. 2013, A&A, 551, A142
Dermer, C. D. 1995, ApJ, 446, L63
Dermer, C. D. & Schlickeiser, R. 2002, ApJ, 575, 667
D'Abrusco, R., Álvarez Crespo, N., Massaro, F., et al. 2019, ApJS, 242, 4
Dunkley, J., Komatsu, E., Nolta, M. R., et al. 2009, ApJS, 180, 306
Evans, P. A., Osborne, J. P., Beardmore, A. P., et al. 2014, ApJS, 210, 8
Falcone, A. 2013, in AAS/High Energy Astrophysics Division, Vol. 13, AAS/High Energy Astrophysics Division #13, 114.07
Falcone, A., Stroh, M., & Pryal, M. 2014, in American Astronomical Society Meeting Abstracts, Vol. 223, American Astronomical Society Meeting Abstracts #223, 301.05
Fichtel, C. E., Bertsch, D. L., Dingus, B., et al. 1993, Advances in Space Research, 13, 637
Finke, J. D., Dermer, C. D., & Böttcher, M. 2008, ApJ, 686, 181
Ghirlanda, G., Ghisellini, G., Tavecchio, F., & Foschini, L. 2010, MNRAS, 407, 791
Ghirlanda, G., Ghisellini, G., Tavecchio, F., Foschini, L., & Bonnoli, G. 2011, MNRAS, 413, 852
Ghisellini, G., Maraschi, L., & Treves, A. 1985, A&A, 146, 204
Ghisellini, G., Righi, C., Costamante, L., & Tavecchio, F. 2017, MNRAS, 469, 255
Ghisellini, G. & Tavecchio, F. 2015, MNRAS, 448, 1060
Ghisellini, G., Tavecchio, F., Foschini, L., et al. 2010, MNRAS, 402, 497
Ghisellini, G., Tavecchio, F., Maraschi, L., Celotti, A., & Sbarrato, T. 2014, Nature, 515, 376
Ghosh, P. & Abramowicz, M. A. 1997, MNRAS, 292, 887
Giannios, D., Uzdensky, D. A., & Begelman, M. C. 2009, MNRAS, 395, L29
Giommi, P., Barr, P., Garilli, B., Maccagni, D., & Pollock, A. M. T. 1990, ApJ, 356, 432
Giroletti, M., Massaro, F., D'Abrusco, R., et al. 2016, A&A, 588, A141
Hartman, R. C., Bertsch, D. L., Bloom, S. D., et al. 1999, ApJS, 123, 79
Hartman, R. C., Böttcher, M., Aldering, G., et al. 2001, ApJ, 553, 683
Healey, S. E., Romani, R. W., Taylor, G. B., et al. 2007, ApJS, 171, 61
Hervet, O., Williams, D. A., Falcone, A. D., & Kaur, A. 2019, ApJ, 877, 26
Impey, C. D. & Neugebauer, G. 1988, AJ, 95, 307
Isobe, N., Sugimori, K., Kawai, N., et al. 2010, PASJ, 62, L55
Jorstad, S. G., Marscher, A. P., Mattox, J. R., et al. 2001, ApJS, 134, 181
Kalberla, P. M. W., Burton, W. B., Hartmann, D., et al. 2005, A&A, 440, 775
Kataoka, J., Yatsu, Y., Kawai, N., et al. 2012, ApJ, 757, 176
Kaur, N., Chandra, S., Baliyan, K. S., Sameer, & Ganesh, S. 2017, ApJ, 846, 158
Landi, R., Bassani, L., Stephen, J. B., et al. 2015, A&A, 581, A57
Landoni, M., Massaro, F., Paggi, A., et al. 2015, AJ, 149, 163
León-Tavares, J., Valtaoja, E., Chavushyan, V. H., et al. 2011, MNRAS, 411, 1127
Lico, R., Giroletti, M., Orienti, M., et al. 2014, A&A, 571, A54
Lister, M. L., Aller, M. F., Aller, H. D., et al. 2013, AJ, 146, 120
Lister, M. L., Homan, D. C., Hovatta, T., et al. 2019, ApJ, 874, 43
Mahony, E. K., Sadler, E. M., Murphy, T., et al. 2010, ApJ, 718, 587
Mao, P., Urry, C. M., Massaro, F., et al. 2016, ApJS, 224, 26
Maraschi, L., Ghisellini, G., & Celotti, A. 1992, ApJ, 397, L5
Marchesini, E. J., Masetti, N., Chavushyan, V., et al. 2016, A&A, 596, A10
Marchesini, E. J., Peña-Herazo, H. A., Álvarez Crespo, N., et al. 2019a, Ap&SS, 364, 5
Marchesini, E. J., Peña-Herazo, H. A., Álvarez Crespo, N., et al. 2019b, Ap&SS, 364, 5
Maselli, A., Massaro, E., Nesci, R., et al. 2010, A&A, 512, A74
Maselli, A., Massaro, F., Cusumano, G., et al. 2013, ApJS, 206, 17
Masetti, N., Sbarufatti, B., Parisi, P., et al. 2013, A&A, 559, A58
Massaro, E., Maselli, A., Leto, C., et al. 2015a, Ap&SS, 357, 75
Massaro, E., Tramacere, A., Perri, M., Giommi, P., & Tosti, G. 2006, A&A, 448, 861
Massaro, F., Álvarez Crespo, N., D'Abrusco, R., et al. 2016, Ap&SS, 361, 337
Massaro, F. & D'Abrusco, R. 2016, ApJ, 827, 67
Massaro, F., D'Abrusco, R., Ajello, M., Grindlay, J. E., & Smith, H. A. 2011a, ApJ, 740, L48
Massaro, F., D'Abrusco, R., Giroletti, M., et al. 2013a, ApJS, 207, 4
Massaro, F., D'Abrusco, R., Giroletti, M., et al. 2013b, ApJS, 207, 4
Massaro, F., D'Abrusco, R., Landoni, M., et al. 2015b, ApJS, 217, 2
Massaro, F., D'Abrusco, R., Paggi, A., et al. 2013c, ApJS, 209, 10
Massaro, F., D'Abrusco, R., Tosti, G., et al. 2012a, ApJ, 750, 138
Massaro, F., D'Abrusco, R., Tosti, G., et al. 2012b, ApJ, 752, 61
Massaro, F., Giommi, P., Tosti, G., et al. 2008a, A&A, 489, 1047
Massaro, F., Giroletti, M., Paggi, A., et al. 2013d, ApJS, 208, 15
Massaro, F., Harris, D. E., & Cheung, C. C. 2011b, ApJS, 197, 24
Massaro, F., Landoni, M., D'Abrusco, R., et al. 2015c, A&A, 575, A124
Massaro, F., Masetti, N., D'Abrusco, R., Paggi, A., & Funk, S. 2014, AJ, 148, 66
Massaro, F., Paggi, A., & Cavaliere, A. 2011c, ApJ, 742, L32
Massaro, F., Paggi, A., Elvis, M., & Cavaliere, A. 2011d, ApJ, 739, 73
Massaro, F., Paggi, A., Errando, M., et al. 2013e, ApJS, 207, 16
Massaro, F., Thompson, D. J., & Ferrara, E. C. 2015d, A&A Rev., 24, 2
Massaro, F., Tramacere, A., Cavaliere, A., Perri, M., & Giommi, P. 2008b, A&A, 478, 395
Massaro, F., Tremblay, G. R., Harris, D. E., et al. 2012c, ApJS, 203, 31
Mastichiadis, A. & Kirk, J. G. 1997, A&A, 320, 19
Mattox, J. R. & Ormes, J. F. 2002, in American Astronomical Society Meeting Abstracts, Vol. 201, 147.02
Mauch, T., Murphy, T., Buttery, H. J., et al. 2003, MNRAS, 342, 1117
Mirabal, N. 2009, arXiv e-prints, arXiv:0908.1389

Moretti, A., Campana, S., Tagliaferri, G., et al. 2004, in Proc. SPIE, Vol. 5165, X-Ray and Gamma-Ray Instrumentation for Astronomy XIII, ed. K. A. Flanagan & O. H. W. Siegmund, 232–240
Mukai, K. 1993, Legacy, vol. 3, p.21-31, 3, 21
Nori, M., Giroletti, M., Massaro, F., et al. 2014, ApJS, 212, 3
Paggi, A., Cavaliere, A., Vittorini, V., D'Ammando, F., & Tavani, M. 2011, ApJ, 736, 128
Paggi, A., Cavaliere, A., Vittorini, V., & Tavani, M. 2009a, A&A, 508, L31
Paggi, A., Massaro, F., D'Abrusco, R., et al. 2013, ApJS, 209, 9
Paggi, A., Massaro, F., Vittorini, V., et al. 2009b, A&A, 504, 821
Paggi, A., Milisavljevic, D., Masetti, N., et al. 2014, AJ, 147, 112
Paiano, S., Franceschini, A., & Stamerra, A. 2017, MNRAS, 468, 4902
Pandey, A., Gupta, A. C., & Wiita, P. J. 2017, ApJ, 841, 123
Peña-Herazo, H. A., Marchesini, E. J., Álvarez Crespo, N., et al. 2017a, Ap&SS, 362, 228
Peña-Herazo, H. A., Marchesini, E. J., Álvarez Crespo, N., et al. 2017b, Ap&SS, 362, 228
Peña-Herazo, H. A., Massaro, F., Chavushyan, V., et al. 2019, Ap&SS, 364, 85
Pian, E., Vacanti, G., Tagliaferri, G., et al. 1998, ApJ, 492, L17
Piner, B. G. & Edwards, P. G. 2014, ApJ, 797, 25
Piner, B. G. & Edwards, P. G. 2018, ApJ, 853, 68
Plotkin, R. M., Markoff, S., Trager, S. C., & Anderson, S. F. 2011, MNRAS, 413, 805
Ricci, F., Massaro, F., Landoni, M., et al. 2015, AJ, 149, 160
Romero, G. E., Cellone, S. A., Combi, J. A., & Andruchow, I. 2002, A&A, 390, 431
Sambruna, R. M., Maraschi, L., & Urry, C. M. 1996, ApJ, 463, 444
Sbarrato, T., Ghisellini, G., Maraschi, L., & Colpi, M. 2012, MNRAS, 421, 1764
Shaw, M. S., Romani, R. W., Cotter, G., et al. 2012, ApJ, 748, 49
Sikora, M., Janiak, M., Nalewajko, K., Madejski, G. M., & Moderski, R. 2013, ApJ, 779, 68
Singh, K. P. & Garmire, G. P. 1985, ApJ, 297, 199
Stecker, F. W., Salamon, M. H., & Malkan, M. A. 1993, ApJ, 410, L71
Stevens, J. A., Litchfield, S. J., Robson, E. I., et al. 1994, ApJ, 437, 91
Stickel, M., Padovani, P., Urry, C. M., Fried, J. W., & Kuehr, H. 1991, ApJ, 374, 431
Stroh, M. C. & Falcone, A. D. 2013, ApJS, 207, 28
Tavecchio, F. & Ghisellini, G. 2016, MNRAS, 456, 2374
Tavecchio, F., Ghisellini, G., Bonnoli, G., & Foschini, L. 2011, MNRAS, 414, 3566
Taylor, G. B., Healey, S. E., Helmboldt, J. F., et al. 2007, ApJ, 671, 1355
Taylor, M. B. 2005, in Astronomical Society of the Pacific Conference Series, Vol. 347, Astronomical Data Analysis Software and Systems XIV, ed. P. Shopbell, M. Britton, & R. Ebert, 29
Taylor, M. B. 2006, in Astronomical Society of the Pacific Conference Series, Vol. 351, Astronomical Data Analysis Software and Systems XV, ed. C. Gabriel, C. Arviset, D. Ponz, & S. Enrique, 666
Tchekhovskoy, A., McKinney, J. C., & Narayan, R. 2009, ApJ, 699, 1789
Tramacere, A., Massaro, E., & Taylor, A. M. 2011, ApJ, 739, 66
Tramacere, A., Massaro, F., & Cavaliere, A. 2007, A&A, 466, 521
Voges, W., Aschenbach, B., Boller, T., et al. 1999, A&A, 349, 389
Wehrle, A. E., Pian, E., Urry, C. M., et al. 1998, ApJ, 497, 178
White, R. L., Becker, R. H., Helfand, D. J., & Gregg, M. D. 1997, ApJ, 475, 479
Woo, J.-H., Urry, C. M., van der Marel, R. P., Lira, P., & Maza, J. 2005, ApJ, 631, 762
Wright, E. L., Eisenhardt, P. R. M., Mainzer, A. K., et al. 2010, AJ, 140, 1868
Xiong, D. R. & Zhang, X. 2014, MNRAS, 441, 3375